The exosphere of Mars can be tracked by a high-spectral resolution telescope, such as the Line Emission Mapper

Jennifer A. Carter, K. Dennerl, K. D. Kuntz, W. Dunn, D. Bodewits, C. M. Jackman, S. F. Sembay, G. Branduardi-Raymont, T. Deskins, Dimitra Koutroumpa, et al.

RAS Techniques and Instruments

RASTAI **3,** 484–490 (2024) https://doi.org/10.1093/rasti/rzae033
Advance Access publication 2024 August 9

The exosphere of Mars can be tracked by a high-spectral resolution telescope, such as the Line Emission Mapper

Jennifer A. Carter [1]★ K. Dennerl,[2] K. D. Kuntz,[3] W. Dunn,[4] D. Bodewits,[5] C. M. Jackman,[6] S. F. Sembay,[1] G. Branduardi-Raymont,[7] T. Deskins,[5] D. Koutroumpa,[8] R. Kraft,[9] C. Lisse [10] S. McEntee,[6,11] S. Wolk[9] and F. S. Porter[12]

[1]*School of Physics and Astronomy, University of Leicester, University Road, Leicester LE1 7RH, UK*
[2]*Max Planck Institute for Extraterrestrial Physics, Giessenbachstraße 1, D-85748 Garching, Germany*
[3]*William H. Miller III, Department of Physics and Astronomy, John Hopkins University, Baltimore, MD 21218, USA*
[4]*Department of Physics and Astronomy, University College London, London, WC1E 6BT, UK*
[5]*Department of Physics, Auburn University, Edmund C. Leach Science Center, Auburn, AL 36849, USA*
[6]*Dublin Institute for Advanced Studies (DIAS), Dunsink Observatory, Dublin, D15 XR2R, Ireland*
[7]*Mullard Space Science Laboratory, University College London, Holbury St Mary, Surrey, RH5 6NT, UK*
[8]*LATMOS, Atmospheres, Environments, Space Observations Laboratory, UVSQ 11 boulevard D'Alembert, Guyancourt F-78280, France*
[9]*Center for Astrophysics, Harvard University, Cambridge, MA 02138, USA*
[10]*John Hopkins University Applied Physics Laboratory, 1100 Johns Hopkins Road, Laurel, MD 20723-6099, USA*
[11]*Trinity College, Dublin, D02 PN40, Ireland*
[12]*X-ray Astrophysical Laboratory, NASA Goddard Space Flight Center, Mail Code 662, Greenbelt, MD 20771, USA*

Accepted 2024 July 18. Received 2024 June 24; in original form 2024 January 15

ABSTRACT

Mars provides our local analogue for unmagnetized terrestrial planets and is thus key to understanding the habitability of exoplanets. The lack of a global magnetic field means that the atmosphere interacts directly with the solar wind, causing significant loss of the atmosphere. While *in situ* measurements provide a wealth of detailed local information, they are limited in deriving the global picture. In contrast, remote X-ray observations can provide important global instantaneous coverage over multiple seasons and sampling different solar wind. Previous XMM–Newton observations have detected significant flux via the solar wind charge exchange emission (SWCX) mechanism from an extended planetary halo, and from atmospheric fluorescence. In contrast, *Chandra* observations only detected a low-luminosity disc and a faint halo. It is postulated that these observational differences are due to transient solar wind with increased heavy ion fractions. Here, we present simulated spectra for the proposed NASA mission Line Emission Mapper, of both halo and disc regions, under quiet and transient solar wind. We show that even under moderate solar wind conditions, both SWCX and fluorescence emission lines are readily detected above the background, providing new insights into the loss of planetary atmospheres and the molecular composition of less well-characterized atmospheric abundances.

Key words: X-rays – Mars – High resolution – microcalorimeter – Instrumentation.

1 INTRODUCTION

The Line Emission Mapper (LEM), is a NASA proposed mission under consideration for launch in the 2030s (Kraft et al. 2022). LEM will likely be located at the Lagrange 1 point in the Earth–Sun system. It will probe the circumgalactic medium and intergalactic medium at soft X-ray energies, over a 30 arcmin diameter field of view at $\geq$10 arcsec angular resolution. The cutting-edge 0.9 eV spectral resolution microcalorimeter array in use within the central 8 arcmin of the field of view allow the faintest emission lines to be disentangled and detected above the X-ray background. Although the primary science goals of LEM are to map distant diffuse extended X-ray emission, LEM will provide significant insight into various Solar System objects, including the planet Mars. LEM will have a dedicated and carefully considered guest observer programme to support such observations.

Mars lacks a global field (and associated intrinsic magnetosphere) and instead possesses crustal fields and an induced magnetosphere. As a result its atmosphere can interact directly with the solar wind, providing, along with comets, an analogue for understanding exoplanets across the cosmos, and for testing theories of atmospheric evolution and loss. Multipoint plasma missions to investigate outstanding questions of the Martian system, including how solar wind driving impacts the dynamics of the magnetosphere and ionosphere, have been proposed (Sánchez-Cano et al. 2022). Remote sensing via global imaging offers an additional perspective and context to any *in situ* measurements. There have been limited X-ray observations of

★ E-mail: jac48@le.ac.uk

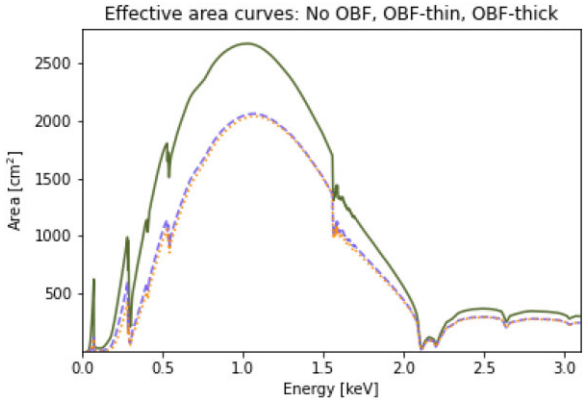

Figure 1. The LEM effective area used in this analysis, without an optical blocking filter (OBF, thick line), and with a thin (dashed line) or thick (dotted line) optical blocking filter, as currently provided by the LEM proposal team, see Section 4.

Mars (see Dennerl (2010) for a review, and Ishikawa et al. (2011)) with the current large-scale X-ray astronomical observatories, the European Space Agency's XMM–Newton (Jansen et al. 2001), NASA's *Chandra* (Weisskopf et al. 2002), and JAXA's Suzaku missions.

For Martian X-rays, the dominant emission processes are charge exchange from the planetary exosphere with the solar wind (SWCX), resulting in line emission characteristic of the incoming solar wind ions, or through fluorescence via scattering of solar X-rays, especially in high density regions of a planet's atmosphere. SWCX was tentatively observed as an extended halo about Mars to about 3 R_M, where 1 R_M is 3390 km, in observations taken by the ACIS-I imaging array on *Chandra* in 2001. The *Chandra* observations were, however, dominated by emissions at a single line energy at 0.65 keV, at the time attributed to O-K_α fluorescence, across the entire planetary disc (Dennerl 2002). Later observations of Mars in 2003, taken by XMM–Newton using the Reflection Grating Spectrometer, separated the SWCX and fluorescent components of the spectra from both the planetary disc and halo regions (Dennerl et al. 2006). Analysis of the XMM–Newton spectra allowed the detection of fluorescence from CO_2 and N_2 molecules from the planetary disc, whereas SWCX line emission was prominent from the exosphere, which becomes evident at energies corresponding to the forbidden line emission resulting from charge exchange between neutrals and solar wind O^{7+} ions. SWCX emission was observed out to around 8 R_M, and there was some suggestion of spatial asymmetries between emissions from oxygen ions and those from carbon, whereby carbon emission was only observed in the planetary Northern hemisphere and generally brighter emissions observed in the north. Levels of SWCX emission are dependent on variations in solar wind flux, composition, or the neutral species participating in the charge exchange process due to cross-sectional differences for the interaction. Charge exchange spectral will differ dependent on the participating neutral species (Mullen et al. 2017), affecting the line ratios between the various transitions present for a particular ion species. The driver for any spatial asymmetries observed is still to be investigated.

The *Chandra* and XMM–Newton observations of Mars differ in total luminosity; ∼4 MW (0.5 MW from the halo and 1.4 MW from the disc) to ∼16 MW (12.8 MW halo, 3.4 MW disc) between the two observations, which has so far been explained due to the large difference in prevailing solar wind conditions (Dennerl 2006, 2010). The *Chandra* observation occurred during a steady period of solar flux, with little to no temporal variability, and no significant variability in the X-ray fluxes from the planet were observed. In contrast, the XMM–Newton observation may have occurred during a passage of several Interplanetary Coronal Mass Ejections (ICMEs) past the planet with only a couple of hours separation (Dennerl 2006). ICMEs are associated with enhanced heavy ion components of the solar wind (Richardson & Cane 2010), and leading edge piled-up high density regions of solar wind plasma, so the passage of these ICMEs would have led to disturbed solar wind conditions in the vicinity of Mars and resulted in enhanced charge exchange emissions above average conditions. There was uncertainty, however, regarding the arrival time of the ICME at Mars, following work to model the propagation of the solar wind to the planet and the resulting charge exchange interactions with planetary neutrals (Koutroumpa et al. 2012). This modelling work used a 3D multiple-species hybrid simulation with a spatial resolution of 130 km. The underlying exosphere model consisted of components of molecular and atomic hydrogen, oxygen, helium, and carbon dioxide. The modelled X-ray emissions were generally compatible with the spatial distributions of the X-ray emissions as observed by XMM–Newton, with the overall hemispheric asymmetries explained by the observing geometry and projection of the Martian bow shock in the field of view. However, the model widely underestimated the observed X-ray luminosities. The solar wind propagation component of the model showed an arrival that occurred at the end of the XMM–Newton observing period, hence, the disturbed solar wind is unable to explain the high X-ray luminosities detected. Later on, Yan et al. (2019) found that unusually highly disturbed solar wind had significantly compressed the induced Martian magnetosphere, which led to the high X-ray luminosities observed. Recently, Liang et al. (2023) have run detailed magnetohydrodynamic simulations of charge exchange at Mars, and these authors compare different neutral atmosphere target atomic and molecular species for a range of collision velocities. They find that charge exchange with atomic hydrogen dominates at altitudes above 400 km. The total X-ray luminosity from this modelling at 6.55 MW is higher than that observed by *Chandra*, but less than that observed by XMM–Newton. The limited observations of Mars so far, and the range of luminosities detected, suggest that X-ray emissions from the planet can be highly variable. The space weather conditions at Mars, as measured by *in situ* plasma on board the *Mars Atmosphere and Volatile Evolution* spacecraft in orbit around the planet, shows modal solar wind densities between 1 and 2 cm^{-2}, modal velocities of approximately 380 kms^{-1}, and modal dynamic pressure at approximately 0.6 nPa (Liu et al. 2021). Extreme density values of approximately 30 cm^{-3} have been detected (Lee et al. 2017). Furthermore, evidence of the impact of Martian dust storms causing detectable changes to the induced magnetosphere boundary on Mars, offers a tantalizing possibility of monitoring sporadic periods of enhanced atmospheric escape causing large-scale changes to Martian exosphere (Regan et al. 2024). Therefore Mars warrants further study sampling different periods of the solar cycle and during the impact of transients to further understand the evolution of the outer atmosphere of Mars under contrasting scenarios.

In this paper, we report on simulated spectra using the available spectral response and effective area files for LEM. We test whether a set of sample emission lines will be discernible from the X-ray sky background under two scenarios; under quiescent incoming solar wind conditions, or under transient solar wind conditions, such as those that might be observed during the passage of an ICME. We use the previous observations made by *Chandra* and XMM–Newton as the basis of our scaling and spectral model. This work was a design and planning study by the LEM Planetary Science Working Group, part of the wider LEM Consortium.

Table 1. Spectral model used in the simulations of Mars halo and disc, adapted from Dennerl et al. (2006). We note the emission process involved, the original incoming solar wind ion species, or the participating molecular species involved, the emission energy, the atomic transition involved, and the photon fluxes used for scaling the model. Note, we take the fluxes (Dennerl et al. 2006), without considering the upper and lower energy bounds in that work.

Index	Label	Emission process	Solar wind ion	Energy (eV)	Transition	Fluxes Disc (10^{-6} cm^{-2} s^{-1})	Fluxes Halo (10^{-6} cm^{-2} s^{-1})
1	C52	CX	C^{6+}	367.6	$2p \rightarrow 1s$	11.0	9.1
2	C45	CX	C^{5+}	378.5	$5p \rightarrow 1s$	2.8	8.4
3	N22	F	N_2	394.0	$3\sigma_g \rightarrow 1s$	5.8	1.4
4	C53	CX	C^{6+}	435.6	$3p \rightarrow 1s$	1.9	7.9
5	C54	CX	C^{6+}	459.4	$4p \rightarrow 1s$	5.7	5.3
6	C55	CX	C^{6+}	470.4	$5p \rightarrow 1s$	2.7	5.5
7	N62	CX	N^{7+}	500.3	$2p \rightarrow 1s$	4.5	7.1
8	CO2b	F	CO_2	523.5	$3\sigma_u \rightarrow 1s$	21.7	3.6
9	CO2a	F	CO_2	527.7	$1\pi_g \rightarrow 1s$	23.2	3.5
10	O6f	CX	O^{7+}	560.9	$2^1P_1 \rightarrow 1^1S_0$	4.2	5.3
11	O6i	CX	O^{7+}	568.5	$2^3P_1 \rightarrow 1^1S_0$	1.2	2.2
12	O6r	CX	O^{7+}	574.0	$2^3S_1 \rightarrow 1^1S_0$	7.0	1.4
13	N63	CX	N^{7+}	593.0	$3p \rightarrow 1s$	2.4	22.0
14	O72	CX	O^{8+}	653.6	$2p \rightarrow 1s$	4.3	7.4
15	O65	CX	O^{7+}	712.5	$5p \rightarrow 1s$	0.4	6.2
16	O74	CX	O^{8+}	817.0	$4p \rightarrow 1s$	0.4	1.6
17	Ne72	F, CX[a]	Ne^{8+}	872.5	$2p \rightarrow 1s$	0.5	3.8

[a] This line is debatably from charge exchange, see the comment in table 2 of Koutroumpa et al. (2012), but here we keep the F assignment to align with the original publication.

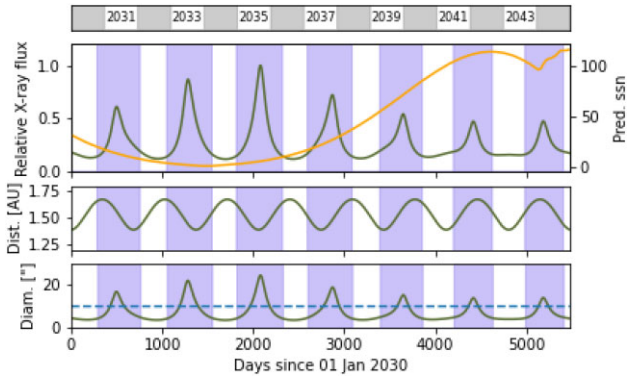

Figure 2. Top to bottom panels show alternate years, relative X-ray flux, heliospheric distance and angular diameter of Mars planetary disc against time. In the panel of relative X-ray flux, we also plot a representative curve, of the predicted number of sunspots for solar cycle 25 and into solar cycle 26, concatenated beyond the limit of the current predictions, see the link in Section 4. Shaded areas mark solar elongation angles that are allowed with the current knowledge of LEM's viewing constraints. The horizontal dashed line in the bottom panel shows the angular resolution of LEM.

2 SIMULATIONS

We simulate various spectra for observations of Mars by LEM, using a spectral model from a previous observation of Mars (Dennerl et al. 2006). For these simulations we used a spectral response file, as provided by the main LEM proposal team. We have run our simulations three times using different effective area files; (1) provided by the main LEM proposal team (see the files listed in Section 4), without an optical blocking filter, (2) using a modified response to simulate a thin optical blocking filter, and (3) using a modified response to simulate a thick optical blocking filter. The optical blocking filter responses were based on filters constructed on a neutral mesh with either a 300 Å Al with 1500 Å polyimide, or a 700 Å Al with 1500 Å polyimide coating, for the thin and thick filters, respectively. Response files are available on request from the main LEM proposal team, as noted in Section 4. We plot the effective area curves for the three filter scenarios in Fig. 1.

For our initial Mars spectral model, we used the lines as listed in Table 1, which has been reworked from Dennerl et al. (2006). In this table, there is a model for both charge exchange from a diffuse extended planetary halo, and fluorescent scattering of solar X-ray photons from the planetary disc. There are 14 charge exchange lines (emission process CX) and 3 fluorescence lines (emission process F) in the model. Lines are listed between 0.365 and 0.880 keV. There are few strong charge exchange lines above this band, and those below this band are currently inaccessible and are therefore of unknown strength. The identifying ion refers to the incoming solar wind ion that takes part in the charge exchange reaction, or the molecular species in respect to the fluorescent lines.

Spectral fitting was performed using the XSPEC fitting package (see Section 4). Given our knowledge of the mean ratios between charge states for a given element and incoming solar wind type, we could set the relative line strengths in our simulations. This was achieved by setting line normalizations relative to the flux ratios of a particular line to that from a reference major emission line. For the O^{7+} triplet (lines 10–12), the normalizations for the intercombination (11) and resonant (12) lines were tied to the forbidden line (10). The other emission line from O^{7+} (15) was also tied to the forbidden line of the oxygen triplet. The O^{8+} lines were tied as (16) to (14). The minor transitions of carbon C^{6+} for lines 4–6 were tied to line 1. Finally, all the major lines; 1–3, 7–9, 10, 14, and 17 were tied relative to the line with the highest flux of the whole spectrum, N^{7+} at 593.0 eV (13).

The spectral model, once input as a whole, was scaled to either a quiescent or transient total flux state, in the energy band 0.365 to 0.880 keV. To do this, we converted the luminosities as quoted in the literature for each state to a future hypothetical observing date for

Table 2. Signal-to-noise ratios for a selection of emission lines for an exposure time of 50 ks, from either the planetary disc model or the halo model. Ratios are listed by the effective area response used in the simulation; with no filter, thin, or thick filter, and by the ambient solar wind conditions, either quiet or transient.

		Disc			Halo		
	Ion	No filter	Thin filter	Thick filter	No filter	Thin filter	Thick filter
Quiet	C52	22.6	16.0	14.7	5.7	4.0	3.7
	N62	20.3	16.3	15.6	8.0	6.5	6.2
	O6f	19.5	15.3	14.8	6.0	4.7	4.6
	O72	21.7	18.1	17.8	8.4	7.0	6.9
Transient	C52	20.8	14.7	13.5	36.0	25.4	23.3
	N62	18.7	15.0	14.4	43.7	35.5	34.6
	O6f	17.9	14.0	13.6	38.7	30.4	29.5
	O72	19.8	16.6	16.3	50.4	42.2	41.3

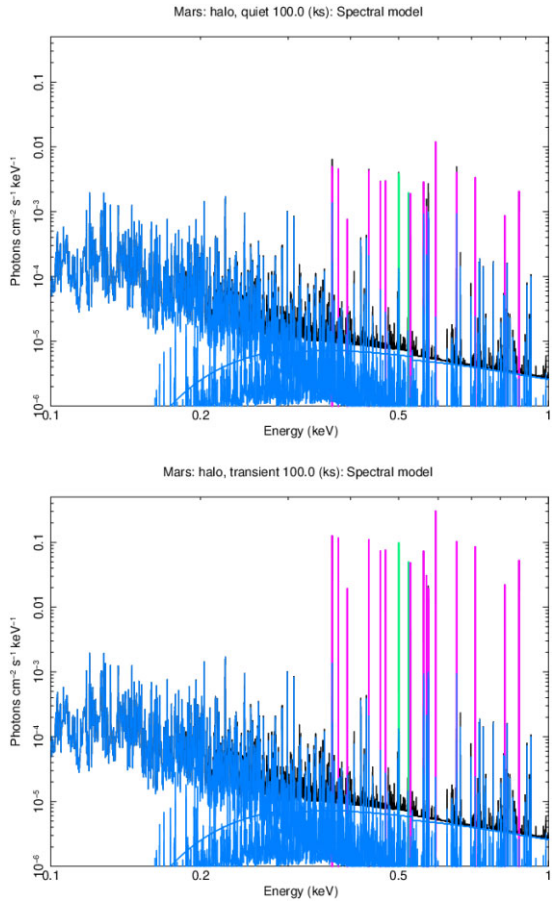

Figure 3. Model spectrum components for the Martian halo on a log–log scale, under quiescent (top) and transient (bottom) conditions. Astronomical sky background components are drawn in blue, fluorescence lines are in green, and charge exchange lines are shown in pink. The combined astronomical sky model spectrum, is shown in black.

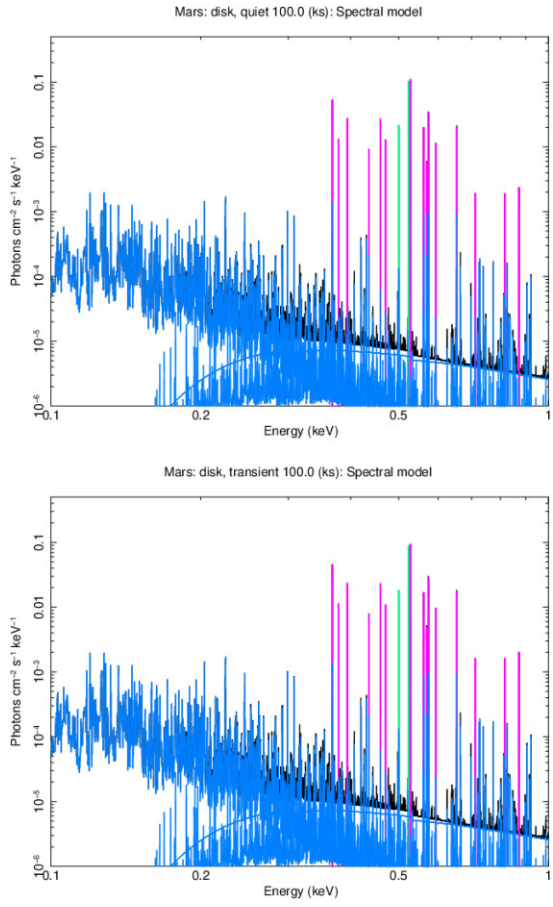

Figure 4. Model spectrum for the Martian disc, under quiescent (top) and transient (bottom) conditions. The colours used are the same in Fig. 3.

LEM; halo and disc for the transient state we use 12.8 and 3.4 MW, respectively. We use planetary ephemeris data from NASA Horizons, see Section 4 to convert between the fluxes obtained in the literature, to LEM which will be positioned at Earth–Sun Lagrangian point 1.

We assume an observation date of 2035 September 1, chosen to minimize the distance from LEM to Mars to 0.38 AU, when Mars is at opposition, providing the best geometric viewing angle for observing Mars at minimum heliospheric distances, giving a correspondingly large angular diameter of the planet and the largest relative X-ray flux. At this distance, the disc will have an extent of approximately 24 arcsec, providing optimal viewing geometries. To observe Mars at opposition, we will have to observe past the Earth, but this will be trivial given the extent of the Lissajous orbit at the Lagrange 1 position. The Earth avoidance angle is currently unknown. Note, that the charge exchange and fluorescence lines will be largely radially symmetric. In Fig. 2, we plot a measure of relative X-ray flux, heliospheric distance, and angular diameter of Mars, against time, with alternate years marked above the plots. We also include a predicted curve of number of sunspots, in orange,

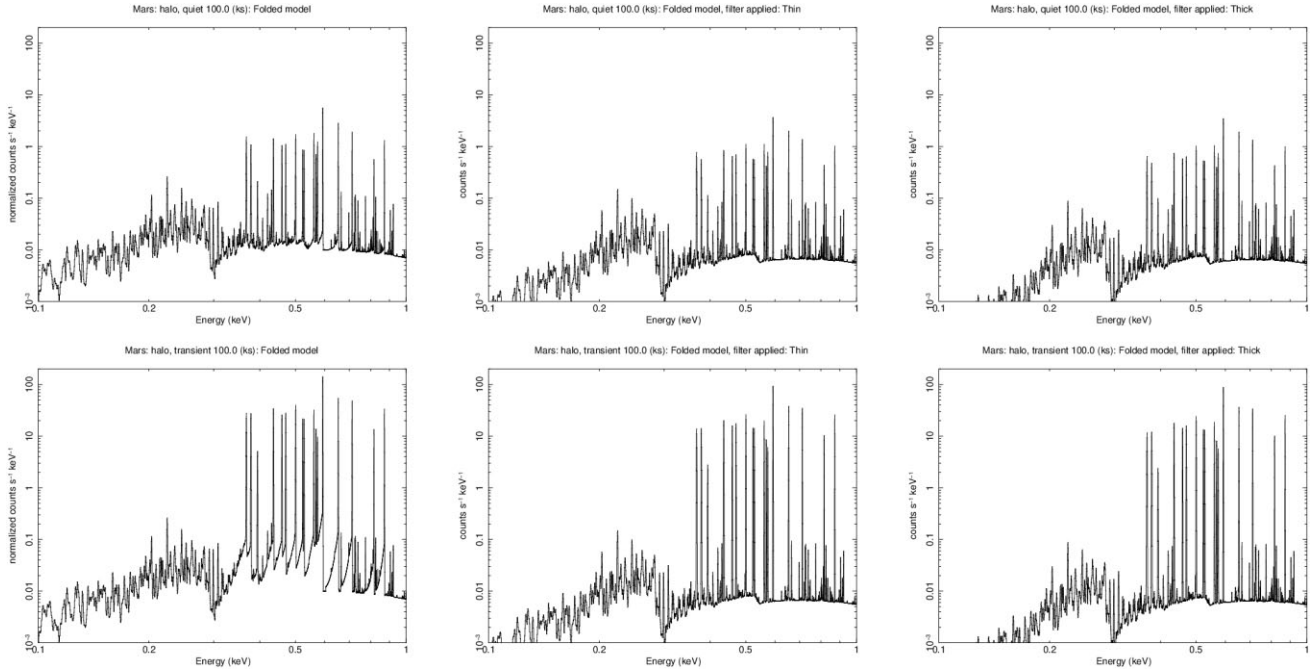

Figure 5. Mars' halo emission spectrum folded through the LEM spectral response, during quiescence (top) and transient (bottom) conditions. Left to right columns show the spectra using the instrumental effective areas as described in the main text: (1) No optical blocking filter, (2) With a thin optical filter, (3) With a thick optical filter.

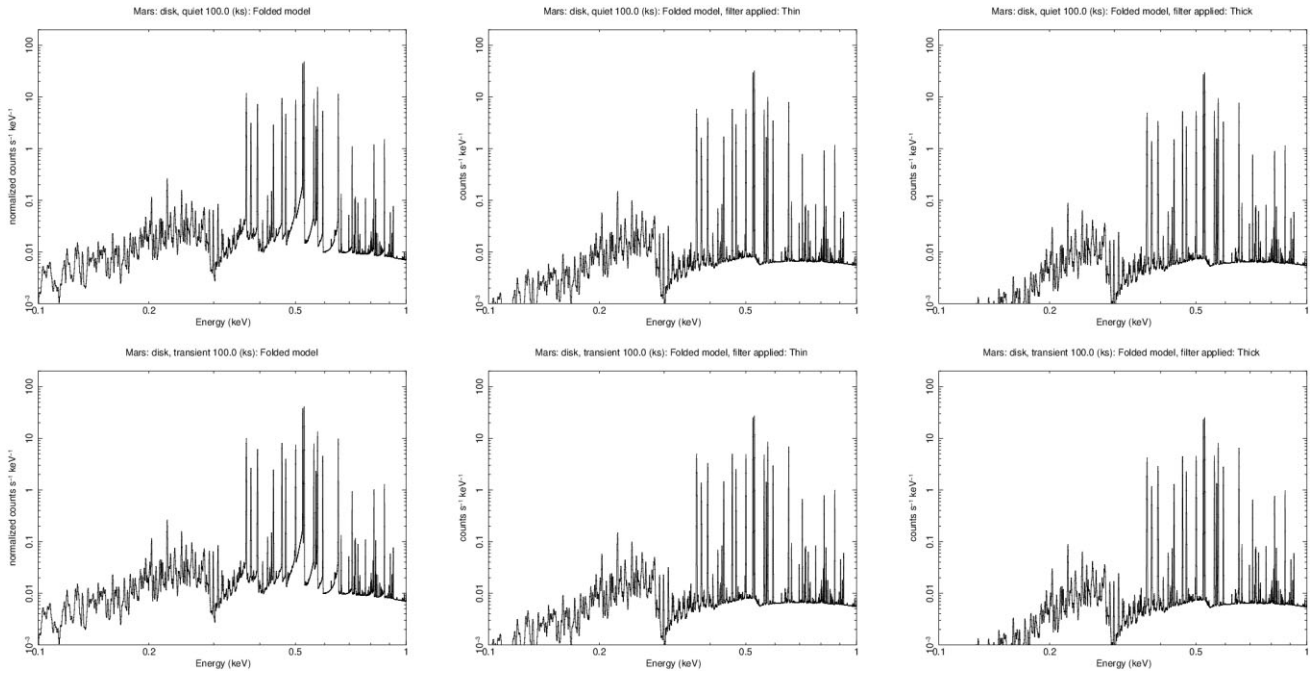

Figure 6. Mars' disc emission spectrum folded through the LEM spectral response, during quiescence (top) and transient (bottom) conditions, and left to right for the instrumental effective areas as described in Fig. 3.

in the same panel as the relative X-ray flux. Lilac shaded areas note solar elongation angles greater than 45 deg and less than 315 deg, to indicate the elongations available to observations by LEM with current knowledge of engineering constraints. However, the caveat at this date is that the solar cycle is likely to be near solar minimum, either between solar cycles 25 and 26, or in the rising phase of solar cycle 26. CMEs can happen at any time during a solar cycle. More extreme transient behaviour, however, is likely in the rising, early phase of an even numbered cycle (Owens et al. 2021). On the other hand, Coronal Interacting Regions, that are relatively periodic at solar minimum, exhibiting approximately two compressions per solar rotation and lasting between 3 and 4 d (Jackman et al. 2004), may inform the observation strategy by offering an opportunity to make comparative observations between rarefied and

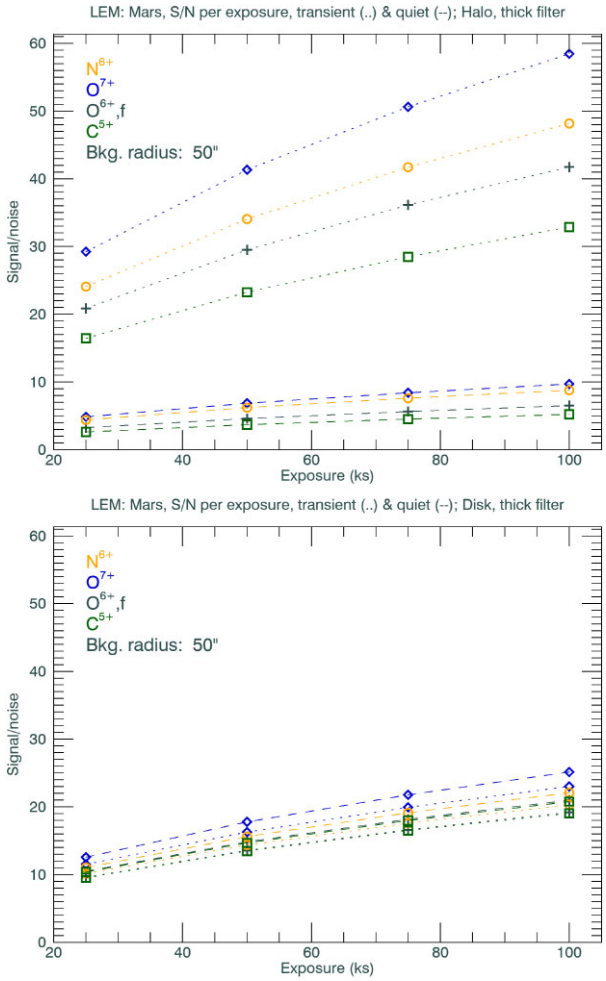

Figure 7. Signal-to-noise ratios for selected emission lines, above the background, plotted by exposure time, for both the Martian halo (top) and disc (bottom) for the effective area response with a thick filter applied. Quiescent times are joined by dashed lines, and transient times by dotted lines. The emission lines of interest in the plots are for C52 (squares), O6f (crosses), O72 (diamonds), and N62 (circles).

dense solar wind if several observations area spread over a 2-week window.

The sky background used was made up of galactic and extragalactic components, and is described in table 2 from Carter, Sembay & Read (2010). The unabsorbed Galactic component was scaled to a flux of 2.1×10^8 erg cm^{-2} s^{-1} sr^{-1} between 0.2 and 10 keV. The absorbed components of the cosmic X-ray background had a flux of 5.5×10^8 erg cm^{-2} s^{-1} sr^{-1}, and the absorbed galactic component had a flux of 1.2×10^8 erg cm^{-2} s^{-1} sr^{-1}, in the same energy range, using a hydrogen column density of 2.79×10^{20} cm^{-2}.

3 RESULTS: MODELLED SPECTRA

In Fig. 3 we plot model spectra for the Martian halo, under both quiescent (top) and transient conditions (bottom). A similar plot is given for the Martian disc in Fig. 4. Here, we plot astronomical sky components in blue. Emission lines are split into fluorescence lines, plotted in green, and charge exchange lines, plotted in pink. For all spectra, emission lines dominate above 0.5 keV. There are no emission lines in the model below 0.37 keV, where the unabsorbed sky background thermal component dominates. Differences between the two disc spectra are barely discernible.

In Figs 5 and 6 we plot the modelled spectra, as shown above in Figs 3 and 4 folded through the instrumental spectral and the three effective area response matrices with no filter applied, or a thin filter, or a thick filter applied. The low energy shoulders of the emission lines are clearly visible.

The simulations were run for a set of different total exposure times. In Fig. 7 we plot the signal to noise of a selection of emission lines, by exposure time for a Mars Halo, top panel, and Mars disc, bottom panel, obtained from the spectra where the thick filter effective area response was applied. The lines shown, with reference to Table 1 are: C52 (green squares), O6f (grey crosses), O72 (blue diamonds), and N62 (yellow circles). We plot both high state (transient) conditions, and also weak (quiescent) conditions with points joined by a dashed line to aid the eye. The signal to noise increase with exposure time for both quiescent and transient cases, as expected. The halo transient case rises steeply, and has much larger values than the quiescent trend. The disc signal-to-noise ratio differences, however, are barely discernible between quiescent and transient states. For both the halo and disc, and under both scenarios, the signal-to-noise ratio is high enough to confidently detect all the example emission lines. Similar behaviour across Fig. 7 is seen for the signal to noise for the optically thin and optically thick blocking filters. We tabulate the signal-to-noise ratios in Table 2 for an example 50 ks exposure. All lines are detectable above the background, including those from the halo under quiet conditions, using the thick filter effective area response.

4 DISCUSSIONS AND CONCLUSIONS

We have produced simulated observations of Mars by the proposed LEM mission, that is currently under consideration by the agencies, basing our work on previous observations of Mars by the large astronomical X-ray telescopes XMM–Newton and *Chandra*. Details of the X-ray spectral fitting package and LEM files used in our work are found in Section 4 below. LEM offers significant improvements in spectral resolution beyond the current astronomical observatories. Although Mars will only subtend a small fraction of LEM's field of view, our motivation was to test the possibilities of this improved spectral resolution in our understanding of Mars' interaction with the solar wind, leading to possible insights into the evolution of the Martian atmosphere.

In this paper, we show that X-ray observations of Mars are feasible under the extremes of both transient and quiescent solar wind conditions for a simulated observing date for the LEM astronomical observatory. X-ray observations of Mars provide a good opportunity to test theories of atmospheric evolution for non-magnetized planets via non-thermal escape mechanisms and to diagnose the molecular composition of under characterized atmospheric abundances. The charge exchange emission process, by nature of the large cross-sections involved, allows for detectable emissions of extended and diffuse planetary exospheres to large distances from the planet.

Mars was set at opposition for the simulations in this paper, and they therefore represent a case with optimal viewing geometries. Depending on the Earth avoidance angle requirements for LEM, a viewing direction perpendicular to the Earth–Sun line may be more realistic. The simulations presented here can be easily adapted for other observing dates.

Routine or sporadic observations of Mars' atmosphere allow monitoring of the atmosphere of an unmagnetized planet over long time-scales, and under variable solar cycle conditions. The LEM team aims to be able to react to transient behaviour of the solar wind,

with a couple of days notice, following the procedures established during missions such as *Chandra*, for example during Director's discretionary time periods, or targets of opportunity. Time-scales of a couple of days are suitable for observing the response of Mars to the passage of a CME.

ACKNOWLEDGEMENTS

JAC is supported by Royal Society grant DHF\R1\211068. WRD is supported by Ernest Rutherford Fellowship: ST/W003449/1. CMJ is supported by a Science Foundation Ireland Award 18/FRL/6199. SFS is supported by Science Technology Facilities Council (STFC) grant ST/X002640/1. For the purpose of open access, the author has applied a Creative Commons Attribution (CC BY) licence to the Author Accepted Manuscript version arising from this submission.

DATA AVAILABILITY

This work makes use of the XSpec spectral fitting package https://heasarc.gsfc.nasa.gov/xanadu/xspec/. Mars ephemeris data were obtained from NASA Horizons https://ssd.jpl.nasa.gov/horizons/app.html. The LEM response files are available from the LEM mission teams on request, and project related resources may be found at https://www.lem⟨plxhyp⟩PLXHYP⟨/plxhyp⟩observatory.org. The response files used at the time of writing were files named lem_09ev_110422.rmf and lem_300522.arf. Predicted sunspot numbers were obtained from NorthWest Research Associates Inc., found at https://spawx.nwra.com/spawx/listpredict.html, which is derived from work by the National Ocenic and Atmosphere Administration, https://www.swpc.noaa.gov/.

REFERENCES

Carter J. A., Sembay S., Read A. M. 2010, MNRAS, 402, 867
Dennerl K., 2002, A&A, 394, 1119
Dennerl K., 2006, Space Sci. Rev., 126, 403
Dennerl K., 2010, Space Sci. Rev., 157, 57
Dennerl K. et al., 2006, A&A, 451, 709
Ishikawa K., Ezoe Y., Ohashi T., Terada N., Futaana Y. 2011, PASJ, 63, S705
Jackman C. M., Achilleos N., Bunce E. J., Cowley S. W. H., Dougherty M. K., Jones G. H., Milan S. E., Smith E. J. 2004, J. Geophys. Res.:Space Phys., 109, A11203
Jansen F. et al., 2001, A&A, 365, L1
Koutroumpa D., Modolo R., Chanteur G., Chaufray J. Y., Kharchenko V., Lallement R. 2012, A&A, 545, A153
Kraft R. et al., 2022, preprint (arXiv:2211.09827)
Lee C. O. et al., 2017, J. Geophys. Res.: Space Phys., 122, 2768
Liang G. Y. et al., 2023, ApJ, 943, 85
Liu D. et al., 2021, ApJ, 911, 113
Mullen P. D., Cumbee R. S., Lyons D., Gu L., Kaastra J., Shelton R. L., Stancil P. C. 2017, ApJ, 844, 7
Owens M. J., Lockwood M., Barnard L. A., Scott C. J., Haines C., Macneil A. 2021, Sol. Phys., 296, 82
Regan C. E. et al., 2024, Planet. Sci. J., 5, 130
Richardson I. G., Cane H. V. 2010, Sol. Phys., 264, 189
Sánchez-Cano B. et al., 2022, Exp. Astron., 54, 641
Weisskopf M. C., Brinkman B., Canizares C., Garmire G., Murray S., Van Speybroeck L. P. 2002, PASP, 114, 1
Yan L., Gao J., Chai L., Zhao L., Rong Z., Wei Y. 2019, ApJ, 883, L38

This paper has been typeset from a TEX/LATEX file prepared by the author.